Spin-1 Weyl point and surface arc state in a chiral phononic crystal

Xiaotian Shi and Jinkyu Yang*
Aeronautics and Astronautics, University of Washington, Seattle, Washington 98195, USA

(Received 20 November 2019; accepted 15 April 2020; published 24 June 2020)

The spin-1 Weyl point is formed by three bands touching at a single point in three-dimensional (3D) momentum space, with two of the bands showing conelike dispersion while the third band is flat. Such a triply degenerate point carries a higher topological charge ±2 and can be described by a three-band Hamiltonian. We first propose a tight-binding model of a 3D Lieb lattice with chiral interlayer coupling to form the spin-1 Weyl point. Then we design a chiral phononic crystal that carries these spin-1 Weyl points and special straight-type acoustic Fermi arcs. We also demonstrate computationally the robust propagation of topologically protected surface states that can travel around a corner or defect without reflection. Our results pave the way to the manipulation of acoustic waves in 3D structures, and they provide a platform for exploring energy transport properties in 3D spin-1 Weyl systems.

DOI: 10.1103/PhysRevB.101.214309

I. INTRODUCTION

In the past decade, Weyl semimetals [1–3] have become a research focus in the field of three-dimensional (3D) topological states, which are characterized by the touching of two bands with linear dispersion in all directions of 3D momentum space, namely the Weyl point. Weyl points behave like monopoles of Berry flux in reciprocal space, which carry a nonzero topological charge (or Chern number) [4]. Such topological invariants result in a robustness of the Weyl points that are stable against small perturbations and cannot be easily gapped. Previous research in Weyl materials has demonstrated a variety of exotic phenomena, such as robust surface states [1] and a chiral anomaly [5]. In parallel, Weyl points have also been realized in other classic systems of electromagnetic [6–10], acoustic [11–16], and stress waves [17,18], leading to novel applications such as negative refraction [14] and the collimation effect [15]. In addition to a single Weyl point with a topological charge (±1), double Weyl points carrying higher topological charges (±2), which are formed by the degeneracy of two bands with quadratic dispersion in a certain momentum plane, have also been discovered [2,8,9,14,17].

Recently, a new type of triply degenerate point of topological charge (±2), referred to as the spin-1 Weyl point [19], has started to attract significant attention. It is formed by the linear degeneracy of three bands having conelike dispersion with a flat band located at the touching point. This can be described by a simple three-band $\mathbf{k}\cdot\mathbf{S}$ Hamiltonian with a spin-1 vector $\mathbf{S}$ [19]. Spin-1 Weyl points have been theoretically predicted in condensed-matter systems [19–22], cold atoms [23–25], and then verified in real materials [26–30]. Yang *et al.* designed and fabricated the first 3D phononic crystal with space group $P2_13$ (No. 198) that carries the acoustic spin-1 Weyl point [31]. They demonstrated experimentally the double Fermi arcs and topologically protected negative refraction of the surface states. However, the unit cell employed is fairly complicated with a nonsymmorphic structure. Also, the system hosts both charge-2 threefold- and fourfold-degenerate points in the Brillouin zone, where the wave propagation is affected by both kinds of degenerate points. The question naturally arises as to whether one could design a simple structure to study the acoustic wave transport properties in 3D spin-1 Weyl systems.

In this paper, we realize the spin-1 Weyl points in a 3D acoustic system. We start with a tight-binding model for a Lieb lattice with chiral interlayer interaction. Previous studies have shown that a 2D Lieb lattice [32], along with other types of 2D lattices such as a $\mathcal{T}_3$ lattice [33] and a kagome lattice [34], can form spin-1 Dirac points. We construct a 3D Weyl structure by stacking up the 2D subsystems with the help of the synthetic gauge flux, which is introduced by the appropriate coupling in the third dimension [11]. We verify that this 3D chiral Lieb lattice can support one pair of spin-1 Weyl points of topological charge ±2 in the first Brillouin zone. The associated Fermi arcs and topological surface arc states are also demonstrated in the proposed architecture. The nearly straight Fermi arcs indicate that we can realize a collimated and robust propagation of surface waves [15].

II. TIGHT-BINDING MODEL OF A 3D LIEB LATTICE

We begin with a tight-binding model of the 3D Lieb lattice with chiral interlayer coupling, as shown in Fig. 1(a). The unit cell has an in-plane lattice constant a and an out-of-plane lattice constant H, containing three sites A (red sphere), B (blue sphere), and C (green sphere). Therefore, we can write the Hamiltonian of the tight-binding model in momentum space as

$$H(\mathbf{k})=\begin{bmatrix} \varepsilon_1+\gamma & 2t_{n1}\cos\left(\frac{k_y a}{2}\right) & 2t_{n1}\cos\left(\frac{k_x a}{2}\right) \\ 2t_{n1}\cos\left(\frac{k_y a}{2}\right) & \varepsilon_2+2t_{n4}\cos(k_y a) & \alpha+i\beta \\ 2t_{n1}\cos\left(\frac{k_x a}{2}\right) & \alpha-i\beta & \varepsilon_2+2t_{n4}\cos(k_x a) \end{bmatrix}.$$

*jkyang@aa.washington.edu

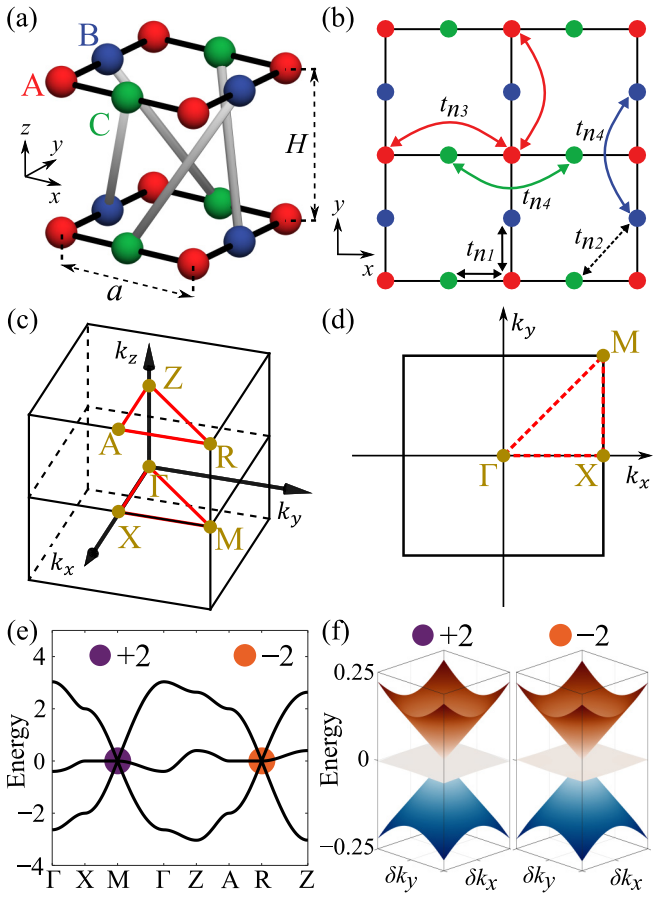

FIG. 1. (a) Schematic of the 3D Lieb lattice with chiral interlayer couplings. (b) Illustration of in-plane short- and long-range intralayer hoppings. (c) First Brillouin zone of the system. (d) 2D reduced reciprocal k_x-k_y plane with fixed $k_z = 0$. (e) Band structure of the three-band Hamiltonian with purple and orange points indicating the spin-1 Weyl points. (f) 3D dispersion surfaces near the spin-1 Weyl points at the M and R points.

Here, ε_1 stands for the on-site potential on A sites, while ε_2 denotes the on-site potential on B and C sites, $\alpha = [t_{n2} + 4t_c\cos(k_z H)]\cos(\frac{k_x a}{2})\cos(\frac{k_y a}{2})$, $\beta = 4t_c\sin(k_z H)\sin(\frac{k_x a}{2})\sin(\frac{k_y a}{2})$, and $\gamma = 2t_{n3}[\cos(k_x a) + \cos(k_y a)]$. t_c represents the interlayer hopping, while t_{ni} highlights the intralayer hopping.

Figure 1(b) provides more details on the definition of different intralayer hopping parameters. Specifically, t_{n1} and t_{n2} are the short-range hopping, which refers to the nearest-neighbor (between A and B/C sites) and next-nearest-neighbor (between B and C sites) hopping, respectively. In this study, we introduce not only short- but also long-range hopping to improve the accuracy of the tight-binding model. To this end, we introduce t_{n3} (t_{n4}), which stands for the long-range hopping between A sites (B/C sites). The first Brillouin zone and the reduced 2D reciprocal k_x-k_y plane are given in Figs. 1(c) and 1(d).

Without loss of generality, we first consider a simplified tight-binding model with only intralayer nearest-neighbor hopping t_{n1} and chiral interlayer hopping t_c. In Fig. 1(e), we show a typical band structure of the tight-binding model along the high-symmetry lines in the first Brillouin zone with hopping parameters $\varepsilon_1 = \varepsilon_2 = 0$, $t_{n1} = 1$, and $t_c = 0.1$. Evidently, the three bands degenerate at the M point as indicated by the purple point in Fig. 1(e). To investigate the topological property of this triply degenerate point, we expand the general form Hamiltonian around the $M(\frac{\pi}{a}, \frac{\pi}{a}, 0)$ point, which gives

$$H(\Delta\mathbf{k}) = \varepsilon S_0 - t_{n1}\Delta k_x S_1 - t_{n1}\Delta k_y S_2 - 4t_c\Delta k_z S_3.$$

Here, $\varepsilon = \varepsilon_1 - 4t_{n3} = \varepsilon_2 - 2t_{n4}$ is the eigenenergy of the triply degenerate point, $\Delta\mathbf{k} = (\Delta k_x, \Delta k_y, \Delta k_z)$ is a small k-vector deviating from the M point, S_0 is the 3×3 unit matrix, and S_1, S_2, S_3 are three of the Gell-Mann matrices given as [35]

$$S_1 = \begin{pmatrix} 0 & 0 & 1 \\ 0 & 0 & 0 \\ 1 & 0 & 0 \end{pmatrix}, \quad S_2 = \begin{pmatrix} 0 & 1 & 0 \\ 1 & 0 & 0 \\ 0 & 0 & 0 \end{pmatrix},$$
$$S_3 = \begin{pmatrix} 0 & 0 & 0 \\ 0 & 0 & -i \\ 0 & i & 0 \end{pmatrix}.$$

Such a linearized Hamiltonian describes a spin-1 Weyl point of topological charge $+2$, which is a natural generalization of the regular Weyl point [19,35]. Note that the triply degenerate points exist only if the system parameters (ε_1, ε_2, t_{n3}, and t_{n4}) satisfy the equation $\varepsilon = \varepsilon_1 - 4t_{n3} = \varepsilon_2 - 2t_{n4}$. This indicates that the spin-1 Weyl point in this model is not guaranteed by the symmetry properties of the unit cell. Instead, it is a result of accidental degeneracy and requires very fine tuning of the system parameters, most importantly the on-site potentials.

Near the degenerate point in Fig. 1(e), the first and third bands have linear dispersion, while the second band remains nearly flat, which is typical behavior of the spin-1 Weyl point. Similarly, there exists another spin-1 Weyl point with topological charge -2 at the corner of the first Brillouin zone (R point). Figure 1(f) shows the 3D dispersion surfaces near the two spin-1 Weyl points, which gives a better visualization of the Weyl cones that interact with a nearly flat band in gray.

III. SPIN-1 WEYL POINT IN PHONONIC CRYSTAL

Although the tight-binding model is just a simple toy model, it provides a keen insight into the physics and a guideline for designing realistic phononic systems. Inspired by the recent work on acoustic type I or type II Weyl points [11,13,15,16], we design a chiral phononic crystal following the stacking-up approach. Each layer of the structure can be viewed as a 2D Lieb lattice that carries a Dirac point, which is intersecting with a flatband. By introducing the appropriate interlayer coupling, we can construct the triply degenerate spin-1 Weyl point in 3D reciprocal space.

Figure 2(a) shows the unit cell of the structure with a lattice constant $a = 20$ mm in the xy plane. The unit cell consists of a scattering pillar and a perforated plate base with slanted air tubes. Figure 2(b) is a top view of the upper pillar, which contains a cylinder (radius $= \sqrt{\frac{b^2+t^2}{2}}$) in the center and four wings. The hollow channels (filled by air) between the neighboring solid pillars form the in-plane acoustic waveguide in analog

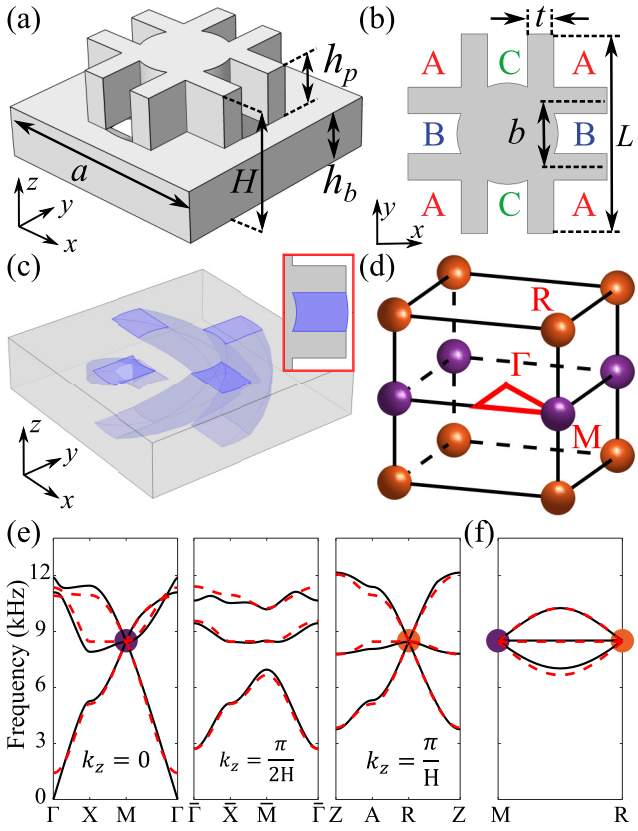

FIG. 2. (a) Schematic of the unit cell of the chiral phononic crystal. (b) Top view of the upper pillar of the unit cell. (c) Lower perforated plate base of the unit cell. (d) Distribution of the spin-1 Weyl points within the first Brillouin zone. (e) Bulk band structure of the phononic crystal in the reduced 2D reciprocal $k_x - k_y$ plane for fixed $k_z = 0$, $k_z = \pi/2H$, and $k_z = \pi/H$. (f) Bulk band structure along the MR direction. The results calculated by the full-wave simulation in COMSOL and the long-range tight-binding model are shown in (e) and (f) as solid black lines and dashed red lines, respectively.

to the 2D Lieb phononic lattice. The wings have width $L = 10\,\text{mm}$ and thickness $t = 2\,\text{mm}$. The distance between the centerlines of the two parallel wings is $b = 5\,\text{mm}$. The colored letters (A, B, and C) give us a rough mapping relation between the in-plane waveguides and the tight-binding model shown in Fig. 1(a). Figure 2(c) shows the perforated plate base. The four purple regions represent the slanted air tubes that bring the chiral interlayer couplings. These holes are generated by sweeping a surface [shown in the Fig. 2(c) inset] in a spiral manner for 90°. The details of the intralayer and interlayer waveguides are demonstrated in Appendix A. Both the upper pillar and the base plate are of height $h_p = h_b = 5\,\text{mm}$, such that the unit cell is of height $H = 10\,\text{mm}$ in total in the z direction.

The distribution of the spin-1 Weyl points in the first Brillouin zone is shown in Fig. 2(d). As we can see, there exists a spin-1 Weyl point with topological charge $+2$ at the M point on the $k_z = 0$ plane and a spin-1 Weyl point carrying topological charge -2 located at the R point on the $k_z = \pm\pi/H$ planes. The topological charges of the Weyl points are numerically calculated by the Wilson loop method [36] (see Appendix B for details). Considering that the Weyl points at the M (R) points are shared by four (eight) neighboring Brillouin zones, there is one pair of spin-1 Weyl points with opposite charges (± 2) existing in the first Brillouin zone.

To confirm the existence of the spin-1 Weyl points, we conduct numerical simulations of the acoustic wave dispersions using the commercial finite-element analysis (FEA) software COMSOL MULTIPHYSICS. We show the computational results of the frequency band structures of the unit cell on a 2D reduced reciprocal plane for fixed $k_z = 0$, $k_z = \pi/2H$, and $k_z = \pi/H$ in Fig. 2(e). For comparison, we also include the results based on the long-range tight-binding model (dashed curves), which are in excellent agreement with the FEA results. See Appendix C for details, including the improvement of the tight-binding model's accuracy by implementing the long-range model over the short-range one.

In Fig. 2(e), we observe that the first three bands of the bulk dispersion diagram are degenerated at the M and R points. While k_z is different from 0 and $\pm\pi/H$, the degeneracy at the Weyl points is broken by the synthetic gauge flux introduced by the chiral interlayer couplings. Such a trend can be observed through the unit-cell band structure along the MR line at the boundary of the first Brillouin zone [see Fig. 2(f)]. When we fix $k_z = \pi/2H$, the degeneracy is lifted, and two band gaps merge between the first three bands. By evaluating the rotational symmetry of the eigenmodes at the high symmetric points in the reduced 2D Brillouin zone [37], we see that the two band gaps are both of nonzero Chern number (-1), which indicates that they are topologically nontrivial. Based on the bulk-edge correspondence of topology, we expect to see topologically protected localized modes at the boundary of the system.

IV. SURFACE ARC STATES AND ACOUSTIC FERMI ARCS

To demonstrate the topologically protected, directional surface arc states in the system, we construct a supercell consisting of 20 unit cells. The strip is finite in the y direction and has hard boundary conditions on the positive and negative y ends. We apply periodic boundary conditions in both the x and z directions. By fixing $k_z = \pi/2H$ and varying k_x from $-\pi/a$ to π/a, we obtain the projected band structures in the x direction, as shown in Fig. 3(a). We can observe that surface arc states emerge in both of the nontrivial band gaps. The red curves represent the modes that are localized at the top ends, while the blue curves stand for the modes localized at the bottom ends. Four localized eigenmodes corresponding to the stars in Fig. 3(a) are plotted in Fig. 3(b). By looking at the slope of the bands that represent the surface arc states, we can determine the sign of their group velocities. We know that the bottom-end (top-end) modes will propagate in the positive (negative) x direction. Then the Fermi arc can be obtained by looking at the equifrequency contour of the band structure of the supercell in the 2D Brillouin zone spanned by k_x and k_z. Here, the fixed frequency works as an equivalent *Fermi energy* in the acoustic systems.

The equifrequency contours at $f = 7.8\,\text{kHz}$ (lying in the first band gap) and $f = 10\,\text{kHz}$ (lying in the second band gap) are plotted in Figs. 3(c) and 3(d), respectively. The colored

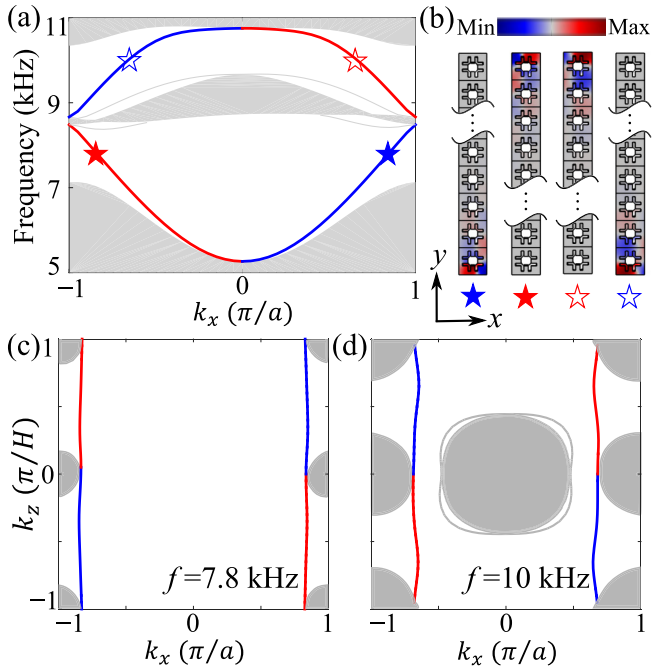

FIG. 3. (a) Projected band structure of the supercell along the x direction for fixed $k_z = \pi/2H$. (b) Calculated eigenmodes of surface arc states at 7.8 or 10 kHz corresponding to the stars in (a). Color intensity represents the magnitude of acoustic pressure field. Equifrequency contours at (c) $f = 7.8$ kHz and (d) $f = 10$ kHz, respectively. The red (blue) lines represent the acoustic Fermi arcs on the positive (negative) xz plane.

lines represent the acoustic Fermi arcs that connect two Weyl points with opposite charges. Specifically, the red (blue) lines stand for the surface Fermi arcs on the positive (negative) xz plane. The gray regions represent the projected bulk bands. As we can see, Fermi arcs exist in both band-gap regions, implying that our structure can support unidirectional surface states in multiple frequency bands. Also, the nearly straight Fermi arcs suggest that the wave packages have group velocity parallel to the x directions, which forms the collimation effect of the surface waves.

We then construct an infinite system to verify the robustness of the surface arc states against the defect and sharp bend (Fig. 4). Such an infinite structure is periodic in the z direction and has finite boundaries in both the x and y directions. We introduce a 3×3 defect on both the right and left boundaries. The top boundary is set to be radiative so that the sound waves can leak out to the outside environment, as marked by the green edge in Fig. 4. A point source is located at the center of the bottom boundary denoted by the red stars. For fixed $k_z = -\pi/2H$ and $f = 7.8$ kHz, we can see that the surface waves only travel in the clockwise direction and can pass around the defect and right angle corner without backscattering [see Fig. 4(a)]. If we set $k_z = +\pi/2H$, the surface waves will travel to the opposite direction [see Fig. 4(b)]. Similarly, the surface arc states at $f = 10$ kHz are demonstrated and confirmed in Appendix D.

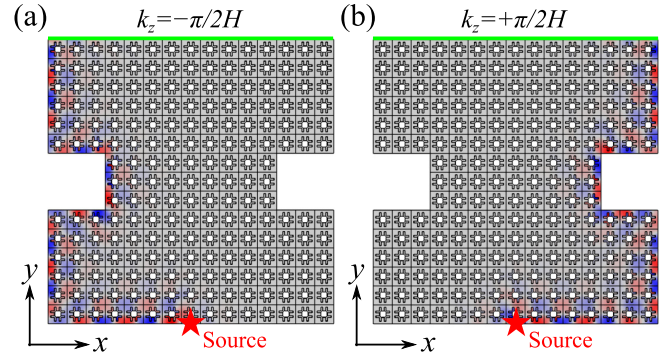

FIG. 4. One-way propagation of the topologically protected surface arc states at $f = 7.8$ kHz for (a) $k_z = -\pi/2H$ and (b) $k_z = +\pi/2H$. Color intensity represents the magnitude of the acoustic pressure field.

V. CONCLUSION

In conclusion, a three-band tight-binding model of a 3D Lieb lattice is introduced to predict the existence of the spin-1 Weyl points. Guided by the tight-binding model, we designed a 3D chiral phononic crystal that carries spin-1 Weyl points with topological charge ± 2 in the first Brillouin zone. We observed a special straight-type acoustic Fermi arc and the collimated robust propagation of topological surface arc states in the system. The key points of this work can be summarized as follows:

(i) We propose a tight-binding model of a 3D Lieb lattice with chiral interlayer hopping. In addition, we include both the short- and long-range hopping terms, which ensures a deeper understanding of the spin-1 Weyl points from the physics aspect.

(ii) While most of the existing structures supporting Weyl points and surface arc states are based on a woodpile- or graphene-based design, our design explores a platform consisting of square-shaped unit cells to study Weyl physics in acoustic systems. Moreover, the unit cell is of simple geometry and is designed with ease of assembly.

(iii) This study reports dual-band topologically protected and collimated surface waves in the spin-1 Weyl structure.

The present results paved the way for manipulating acoustic waves in a 3D structure, which can be potentially extended to other artificial systems of photonic lattices [38] and mechanical lattices [39].

ACKNOWLEDGMENTS

We thank Professor Jiun-Haw Chu at the University of Washington for fruitful discussions. X.S. and J.Y. are grateful for the financial support from the US National Science Foundation (CAREER1553202 and EFRI-1741685).

APPENDIX A: VIEWS OF THE FILLING AIR IN THE UNIT CELL

In this Appendix, we provide more details of the filling air in the unit cell. Figure 5(a) contains the oblique and top views of the chiral interlayer air channels, which introduces the

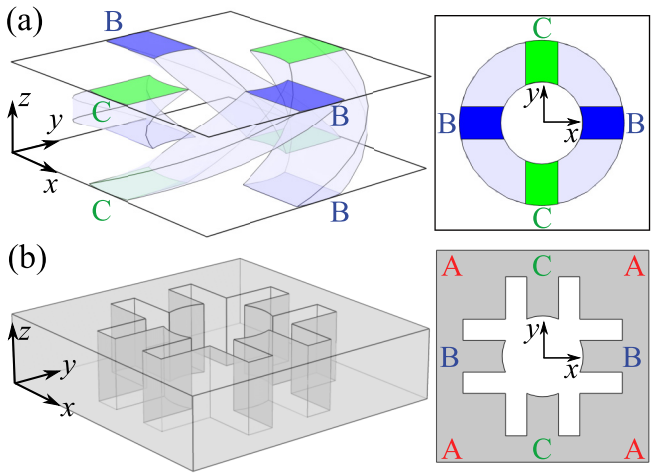

FIG. 5. Oblique and top views of (a) chiral interlayer air channels and (b) intralayer acoustic waveguide. The colored letters and surfaces demonstrate the mapping relations between the real phononic crystal unit cell and the effective tight-binding model. In (b), the gray area represents the in-plane acoustic waveguide, while the white area indicates the solid pillar.

synthetic gauge flux in the system. As we can see, all the top holes rotate 90° in a spiral manner with respect to the bottom holes. Figure 5(b) shows the in-plane 2D acoustic waveguide, which is formed by the air between two neighboring perforated plates. The scattering pillars help to form an effective 2D Lieb lattice. Then, these neighboring 2D waveguides are coupled by the interlayer air channels, thereby forming a 3D chiral Lieb lattice.

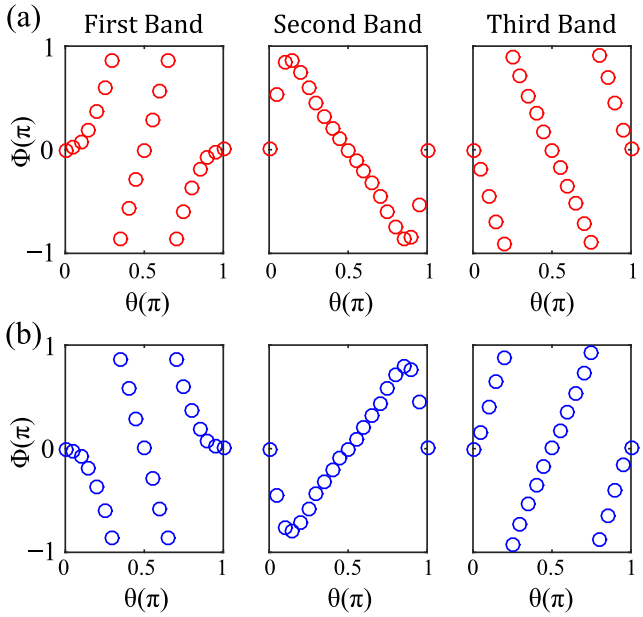

FIG. 6. Evolution of the Wannier centers on the spheres enclosing the spin-1 point. (a) Wannier centers for the first three bands near the M point. (b) The same as (a) for the first three bands near the R point.

APPENDIX B: CALCULATION OF THE CHERN NUMBERS WITH THE WILSON LOOP METHOD

The Chern number (or topological charge) can be calculated by integrating Berry curvature on a closed surface enclosing a band degenerate point. Following the method in Refs. [3,10,31], we numerically determine the Chern number by tracking the evolution of the Wannier centers on a sphere surrounding the spin-1 Weyl point using the Wilson loop method [36]. The calculated Wannier centers on the horizontal loops varying from the north pole to the south pole of the enclosing sphere are presented in Fig. 6. As we can see in Fig. 6(a), the Wannier centers of the spin -1 Weyl point at the M point for the first, second, and third bands shift by $+4\pi$, 0, and -4π, respectively. This implies that such a spin-1 Weyl point has a positive charge of $+2$. Similarly, by looking at Fig. 6(b), we can conclude that there exists a spin-1 Weyl point of charge -2 located at the R point in the first Brillouin zone.

APPENDIX C: UNIT-CELL BAND STRUCTURE CALCULATED BY THE TIGHT-BINDING MODEL AND FULL-WAVE SIMULATIONS

In Fig. 7, we compare the frequency band structures of the unit cell obtained by tight-binding models and the full-wave simulations using COMSOL MULTIPHYSICS. The solid black lines are the results of FEA simulations, which is the same as those plotted in Figs. 2(e) and 2(f). The results of the simplified (i.e., the short-range model with $t_{n2} = t_{n3} = t_{n4} = 0$) and the full (i.e., long-range) three-band tight-binding model are shown as blue dotted and red dashed lines, respectively. The hopping parameters used in a tight-binding model of both cases are determined by fitting the results with the results of COMSOL full-wave simulations. As we can see in Fig. 7, the simplified Hamiltonian (blue dotted line) only works within a small range near the spin-1 Weyl point with the fitting parameters given as $\varepsilon_1 = \varepsilon_2 = 8.516$, $t_{n1} = -1.524$, and $t_c = -0.410$. However, by taking into account more hopping terms, the full tight-binding model (red dashed line) can capture the band structures of real phononic crystal very well in the whole Brillouin zone. Here, we set $\varepsilon_1 = 8.5448$, $\varepsilon_2 = 7.9962$, $t_{n1} = -1.436$, $t_{n2} = -0.509$, $t_{n3} = -0.232$, $t_{n4} = 0.021$, and $t_c = -0.448$ in the full tight-binding model calculation.

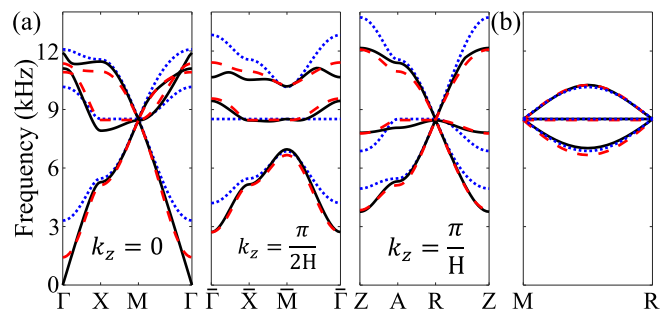

FIG. 7. Bulk band structure of the unit cell obtained by tight-binding models and full-wave simulations in the reduced 2D reciprocal k_x-k_y planes and K-H lines in the first Brillouin zone.

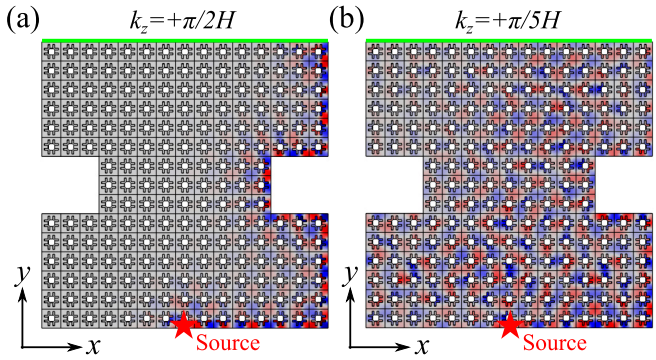

FIG. 8. Surface arc states at $f = 10\,\text{kHz}$, which lies in the second topological nontrivial band gap for (a) $k_z = +\pi/2H$ and (b) $k_z = +\pi/5H$. Color intensity represents the magnitude of the acoustic pressure field.

APPENDIX D: SURFACE STATES AT $f = 10\,\text{kHz}$

In the body of the paper, we show the equifrequency contours of a supercell at $f = 10\,\text{kHz}$ in Fig. 3(d). It is clear that, for several k_z ranges, the structure supports bulk modes and surface modes simultaneously. In this case, we can hardly excite the clear surface modes since they are coupled with the bulk modes and will easily leak to the bulk. To demonstrate such an effect, we conduct numerical simulations under surface excitation at $f = 10\,\text{kHz}$ for $k_z = +\pi/2H$ or $k_z = +\pi/5H$ (see Fig. 8). Similar to the setup in the main context, the structure is infinite in the z direction with a radiative boundary placed on the top edge, denoted by the green line. For $k_z = +\pi/2H$, the surface states can be clearly observed as all the energy is well-confined to the boundary of the structure. However, when we set $k_z = +\pi/5H$, we can barely see the surface waves near the excitation point, and the energy quickly leaks into the bulk of the system.

[1] X. Wan, A. M. Turner, A. Vishwanath, and S. Y. Savrasov, Phys. Rev. B **83**, 205101 (2011).

[2] C. Fang, M. J. Gilbert, X. Dai, and B. A. Bernevig, Phys. Rev. Lett. **108**, 266802 (2012).

[3] A. A. Soluyanov, D. Gresch, Z. Wang, Q. Wu, M. Troyer, X. Dai, and B. A. Bernevig, Nature (London) **527**, 495 (2015).

[4] Z. Fang, N. Nagaosa, K. S. Takahashi, A. Asamitsu, R. Mathieu, T. Ogasawara, H. Yamada, M. Kawasaki, Y. Tokura, and K. Terakura, Science **302**, 92 (2003).

[5] H. B. Nielsen and M. Ninomiya, Phys. Lett. B **130**, 389 (1983).

[6] L. Lu, L. Fu, J. D. Joannopoulos, and M. Soljačić, Nat. Photon. **7**, 294 (2013).

[7] L. Lu, Z. Wang, D. Ye, L. Ran, L. Fu, J. D. Joannopoulos, and M. Soljačić, Science **349**, 622 (2015).

[8] W.-J. Chen, M. Xiao, and C. T. Chan, Nat. Commun. **7**, 13038 (2016).

[9] M.-L. Chang, M. Xiao, W.-J. Chen, and C. T. Chan, Phys. Rev. B **95**, 125136 (2017).

[10] Q. Wang, M. Xiao, H. Liu, S. Zhu, and C. T. Chan, Phys. Rev. X **7**, 031032 (2017).

[11] M. Xiao, W.-J. Chen, W.-Y. He, and C. T. Chan, Nat. Phys. **11**, 920 (2015).

[12] Z. Yang and B. Zhang, Phys. Rev. Lett. **117**, 224301 (2016).

[13] F. Li, X. Huang, J. Lu, J. Ma, and Z. Liu, Nat. Phys. **14**, 30 (2018).

[14] H. He, C. Qiu, L. Ye, X. Cai, X. Fan, M. Ke, F. Zhang, and Z. Liu, Nature (London) **560**, 61 (2018).

[15] H. Ge, X. Ni, Y. Tian, S. K. Gupta, M.-H. Lu, X. Lin, W.-D. Huang, C. T. Chan, and Y.-F. Chen, Phys. Rev. Appl. **10**, 014017 (2018).

[16] B. Xie, H. Liu, H. Cheng, Z. Liu, S. Chen, and J. Tian, Phys. Rev. Lett. **122**, 104302 (2019).

[17] Y.-T. Wang and Y.-W. Tsai, New J. Phys. **20**, 083031 (2018).

[18] X. Shi, R. Chaunsali, F. Li, and J. Yang, Phys. Rev. Appl. **12**, 024058 (2019).

[19] B. Bradlyn, J. Cano, Z. Wang, M. G. Vergniory, C. Felser, R. J. Cava, and B. A. Bernevig, Science **353**, aaf5037 (2016).

[20] P. Tang, Q. Zhou, and S.-C. Zhang, Phys. Rev. Lett. **119**, 206402 (2017).

[21] G. Chang, S.-Y. Xu, B. J. Wieder, D. S. Sanchez, S.-M. Huang, I. Belopolski, T.-R. Chang, S. Zhang, A. Bansil, H. Lin *et al.*, Phys. Rev. Lett. **119**, 206401 (2017).

[22] T. Zhang, Z. Song, A. Alexandradinata, H. Weng, C. Fang, L. Lu, and Z. Fang, Phys. Rev. Lett. **120**, 016401 (2018).

[23] Y.-Q. Zhu, D.-W. Zhang, H. Yan, D.-Y. Xing, and S.-L. Zhu, Phys. Rev. A **96**, 033634 (2017).

[24] I. C. Fulga, L. Fallani, and M. Burrello, Phys. Rev. B **97**, 121402(R) (2018).

[25] H. Hu, J. Hou, F. Zhang, and C. Zhang, Phys. Rev. Lett. **120**, 240401 (2018).

[26] H. Miao, T. T. Zhang, L. Wang, D. Meyers, A. H. Said, Y. L. Wang, Y. G. Shi, H. M. Weng, Z. Fang, and M. P. M. Dean, Phys. Rev. Lett. **121**, 035302 (2018).

[27] D. Takane, Z. Wang, S. Souma, K. Nakayama, T. Nakamura, H. Oinuma, Y. Nakata, H. Iwasawa, C. Cacho, T. Kim *et al.*, Phys. Rev. Lett. **122**, 076402 (2019).

[28] Z. Rao, H. Li, T. Zhang, S. Tian, C. Li, B. Fu, C. Tang, L. Wang, Z. Li, W. Fan *et al.*, Nature (London) **567**, 496 (2019).

[29] D. S. Sanchez, I. Belopolski, T. A. Cochran, X. Xu, J.-X. Yin, G. Chang, W. Xie, K. Manna, V. Süß, C.-Y. Huang *et al.*, Nature (London) **567**, 500 (2019).

[30] N. B. M. Schröter, D. Pei, M. G. Vergniory, Y. Sun, K. Manna, F. de Juan, J. A. Krieger, V. Süss, M. Schmidt, P. Dudin *et al.*, Nat. Phys. **15**, 759 (2019).

[31] Y. Yang, H.-x. Sun, J.-p. Xia, H. Xue, Z. Gao, Y. Ge, D. Jia, S.-q. Yuan, Y. Chong, and B. Zhang, Nat. Phys. **15**, 645 (2019).

[32] R. Shen, L. B. Shao, B. Wang, and D. Y. Xing, Phys. Rev. B **81**, 041410(R) (2010).

[33] D. Bercioux, D. F. Urban, H. Grabert, and W. Häusler, Phys. Rev. A **80**, 063603 (2009).

[34] D. Green, L. Santos, and C. Chamon, Phys. Rev. B **82**, 075104 (2010).
[35] W. Beugeling, J. C. Everts, and C. Morais Smith, Phys. Rev. B **86**, 195129 (2012).
[36] R. Yu, X. L. Qi, A. Bernevig, Z. Fang, and X. Dai, Phys. Rev. B **84**, 075119 (2011).
[37] C. Fang, M. J. Gilbert, and B. A. Bernevig, Phys. Rev. B **86**, 115112 (2012).
[38] J. Mei, Y. Wu, C. T. Chan, and Z.-Q. Zhang, Phys. Rev. B **86**, 035141 (2012).
[39] H. Zhu and F. Semperlotti, Phys. Rev. Appl. **8**, 064031 (2017).